JGR Atmospheres

RESEARCH ARTICLE
10.1029/2019JD031899

Key Points:
- Model depicts large cold bias at deep subsurface temperature (SUBT) during summer over North America due to weaker seasonal change in summer
- West of Rocky Mountains, SUBT effect on land surface temperature is largely overruled by stronger upstream marine influence from the Pacific
- Over the central Great Plains, SUBT is a major cause for severe cold LST bias during summer in simulation and reforecasts

Supporting Information:
- Supporting Information S1

Correspondence to:
R. P. Shukla,
rshukla2@gmu.edu

Citation:
Shukla, R. P., & Huang, B. (2020). Cumulative influence of summer subsurface soil temperature on North America surface temperature in the CFSv2. *Journal of Geophysical Research: Atmospheres*, *125*, e2019JD031899. https://doi.org/10.1029/2019JD031899

Received 24 OCT 2019
Accepted 29 FEB 2020
Accepted article online 5 MAR 2020

Cumulative Influence of Summer Subsurface Soil Temperature on North America Surface Temperature in the CFSv2

Ravi P. Shukla[1] **and Bohua Huang**[1,2]

[1]Center for Ocean-Land-Atmosphere Studies, George Mason University, Fairfax, VA, USA, [2]Department of Atmospheric, Oceanic, and Earth Sciences, George Mason University, Fairfax, VA, USA

Abstract Analyzing a long simulation and a set of seasonal reforecasts of the Climate Forecast System version 2 (CFSv2), this study demonstrates a large model cold bias in the deep soil layer (100–200 cm) over most of North America continent during summer due to weaker seasonal change in summer. The summer subsurface temperature (SUBT) cold bias influences the land surface temperature (LST) during the summer and subsequent seasons in different ways over different geographical regions in North America: West of the Rocky Mountains, the SUBT's effect on LST is largely overruled by the stronger upstream marine influence from the Pacific. Over the central Great Plains, however, it is a major cause for severe cold LST bias during summer in the model simulation and reforecasts. As a result, model underestimates sensible heat flux into the atmosphere but overestimates latent heat flux. The latter may contribute to an excessive summer rainfall in the region. Over the northeast region, the SUBT cold bias persists to August and September, which causes an additional surface cooling in the fall and helps to bring LST to the freezing point early. This sets up the stage for a prolonged snow-albedo feedback. In particular, the model long simulation that passes through previous summer and fall demonstrates longer persistence of snow cover over the northeast region than reforecasts initialized in late winter and spring do. A cold bias of the water temperature in the North Atlantic seems also to play a role to prolong cold bias in the northeast region.

1. Introduction

Despite the significant improvement in representing the physical processes that produce land surface properties in state-of-the-art general circulation models, including snow, heat fluxes, land surface temperature (LST), soil moisture, and vegetation, a number of systematic biases and uncertainties of these properties persist (Douville, 2010; Dutra et al., 2011; Kim & Wang, 2007; Koster et al., 2004, 2011; Santanello et al., 2018; Seneviratne et al., 2006, 2010; van den Hurk et al., 2011, 2012). The inadequate representation of essential processes determining the propagation of information through the hydrological cycle in the general circulation models, as well as insufficient observations that are used to initialize land surface models, is a major cause for large bias in the mean climate and inaccurate evolution of interannual variations, which inevitably affects the prediction skill of air temperature, precipitation, and other surface properties (Delworth & Manabe, 1989; Douville, 2010; Guo et al., 2006; Koster et al., 2010, 2011; Koster & Suarez, 2003; Roesch, 2006; Roundy et al., 2014; Seneviratne et al., 2010; Shukla et al., 2019).

It has long been recognized that the interaction between snow cover and atmosphere can affect the fundamental climate in winter through positive snow-albedo feedback (Dickinson, 1983). The soil moisture anomalies generated by the abnormal snow melting process in the spring can also affect the climate in the following summer through its prolonged hydrologic effect (Barnett et al., 1988; Broxton et al., 2017; Cohen & Rind, 1991; Foster et al., 1983; Furtado et al., 2015; Hahn & Shukla, 1976; Shukla & Mintz, 1982; Yasunari et al., 1991). However, the influence of land subsurface soil temperature (SUBT) on climate and its variability has been less discussed in state-of-the-art coupled general circulation models until recently (e.g., Shukla et al., 2019). A few studies studied the SUBT influence using atmospheric general circulation model (AGCM) and regional climate mode (Mahanama et al., 2008; Fan, 2009; Wu & Zhang, 2014; Xue et al., 2012, 2016, 2018). Using an AGCM forced with prescribed climatological annual cycle of sea surface temperature (SST), Mahanama et al. (2008) conducted experiments with specified or interactive SUBT to

explore the influence of subsurface soil temperature variability on the variability of air temperature. They found that interactive subsurface soil temperature significantly increases surface air temperature variability in most regions. Using the Weather Research and Forecasting model, Wu and Zhang (2014) found that the SUBT feedback plays an important role in amplifying summer surface air temperature variability over the arid/semiarid regions of East Asia, but its influence on precipitation variability is weaker. Using observational data sets, Xue et al. (2012, 2016) found that springtime LST/SUBT anomaly in the northwest United States is significantly correlated with the summer rainfall and temperature changes in the Southern Plains. They confirmed this relationship using AGCM simulations, demonstrating the existence of a long-distance delayed effect from the land temperature in the western United States to the seasonal climate in the southeast. Using an AGCM and a regional climate model, Xue et al. (2018) further explored the relationship between spring LST/SUBT anomalies over the western high-elevation areas in North America and East Asia and late spring/summer droughts or floods in their downstream regions.

Many previous studies have used the National Centers for Environmental Prediction (NCEP) Coupled Forecast System version-2 (CFSv2; Saha et al., 2014) to evaluate the seasonal prediction and simulation of El Niño–Southern Oscillation, Asian summer monsoon and other important atmospheric and oceanic processes in the reforecasts and long-term simulations (Peng et al., 2012; Shukla & Huang, 2015; Dirmeyer & Halder, 2017; Shukla et al., 2017; Huang et al., 2017; Broxton et al., 2017; Shukla, Huang, Dirmeyer, & Kinter, 2019, Shukla, Huang, Dirmeyer, Kinter, Shin, & Marx, 2019, and papers cited therein). Using NCEP CFSv2 Reanalysis and Reforecast (CFSRR; Saha et al., 2014), He et al. (2016, 2018) demonstrated that CFSv2 reproduces the spatial distribution of snow cover fraction (SCF) climatology in April at 0 lead month and snow water equivalent (SWE) during spring for a lead time of 1–3 months in Eurasia. As lead time increases, the model depicts excessive bias of SCF and SWE over Eurasia. Our previous study (Shukla, Huang, Dirmeyer, & Kinter, 2019) demonstrated that CFSv2 produces excessive snow cover and water equivalent, as well as surface albedo in Eurasia throughout spring due to an overactive snow-albedo feedback. The excessive snow amount and its corresponding cold bias in LST also prolong the spring snow melting to early summer, which significantly influences the model-simulated summer climate state in Eurasia. More recently, Shukla, Huang, Dirmeyer, Kinter, Shin, and Marx (2019) further showed that CFSv2 underestimates the amplitude of seasonal cycle in the deep soil temperature in 100–200 cm, resulting in a severe cold SUBT bias during summer in western Eurasia although its winter bias is relatively small. This systematic error of the summer SUBT can influence the subsequent seasonal transition and perpetuates the surface climate state significantly. Specifically, as the solar radiation reduces quickly in early fall, the persistent cold bias in the model's deep soil temperature causes a faster temperature reduction in the upper soil layer and may bring LST down to freezing point early in western Eurasia. As a result, early snow falling on the ground does not melt but start accumulating.

We believe that these error sources (i.e., excessive snow-albedo feedback and summer SUBT cold bias) as identified in Shukla, Huang, Dirmeyer, Kinter, Shin, and Marx (2019) and Shukla, Huang, Dirmeyer, & Kinter (2019) originate from inadequate treatment of land model physics, which may also have similar effects in other major continental areas. Therefore, it is useful to examine what potential influences these error sources may have on the climate state in North America, another large landmass in the Northern Hemisphere. There have been some previous studies examining the influences of land-atmosphere interaction on seasonal prediction in the United States. Analyzing CFSRR, Roundy et al. (2014) demonstrated the importance of correctly characterizing land-atmosphere interactions in order to produce accurate and consistent forecasts for intense droughts years in the United States. They found that land-atmosphere coupling in CFSRR tends toward a wet regime for most areas of the contiguous United States except for the southwest, where a large increase in dry coupling occurs during drought years. Broxton et al. (2017) found that CFSRR initialized in winter (e.g., on 1 January) depicts more SWE in April–June than reforecasts made later (e.g., on 1 April) do. Correspondingly, the earlier forecasts show larger cold bias than the later ones. They attributed these biases to model deficiencies in treating subscale physical processes in the atmospheric (e.g., radiative transfer) and/or land (e.g., snow parameterization) components in CFSv2.

In this paper, we systematically explore the influences of SUBT on LST and snow properties in the subregions of North America using a long CFSv2 simulation and a set of seasonal reforecasts. We found that, in contrast to the large landmass in Eurasia, where the land surface and subsurface condition is a predominant factor, the narrower dimensions of North America adapt the SUBT influence differently in different regions.

In the northeast region, the cold bias of SUBT at 100–200 cm depth from July to September affects the snow properties (e.g., SCF) in the following October to November, initiating an excessive snow-albedo feedback in winter. This largely conforms to the SUBT influence in Eurasia. Moreover, a marine influence from the neighboring North Atlantic may also play a role since the near-freezing water temperature due to a cold SST bias may be another factor for delayed snow melting over the northeast region from April to June in long simulation. Over the Central Great Plains, the cold bias of SUBT from deep soil layer to upper soil layer may cause the regional LST bias during summer. Further to the west, however, the impact of SUBT is largely negligible due to the stronger upstream marine influence from the Pacific.

The remainder of this paper is organized as follows. Section 2 briefly describes the NCEP CFSv2, the experimental design, and verification data,sets. Section 3 presents mean state bias in spring and summer over North America in a long model simulation. Section 4 describes a possible cause for delayed snow melting from March to June over the northeast region, and early appearance of snow cover and excessive snow amount on the ground in this area during October and November. Section 5 describes distinct responses of LST and snow properties to SUBT in the three subregions of North America. Summary and discussion are given in section 6.

2. Model Description, Experimental Design, and Observational Data Sets

The coupled general circulation models used in this study is NCEP CFSv2 (Saha et al., 2014), which includes atmospheric, oceanic, sea ice, and land components. The atmospheric component has a spectral horizontal resolution of T126 (roughly equivalent to a 105-km grid spacing) and 64 vertical levels in a hybrid sigma-pressure coordinate. The oceanic component is the Geophysical Fluid Dynamics Laboratory Modular Ocean Model (MOM) version 4 (MOM4; Griffies et al., 2004), which is configured for the global ocean with a horizontal grid of 0.5° × 0.5° poleward of 30°S/30°N and meridional resolution increasing gradually to 0.25° between 10°S and 10°N (nominally referred to as 0.5° resolution). Vertically, it has 40 levels in a z coordinate, with 27 levels within the upper 400 m and the maximum depth at approximately 4.5 km. The sea ice component is a three-layer global interactive dynamical sea-ice model with predicted fractional ice cover and thickness (Winton, 2000). The land surface component is the Noah land surface model. Directly coupled to the atmospheric component, the Noah land surface model is a computationally efficient model of intermediate complexity for use in operational weather and seasonal prediction models (Ek et al., 2003).

In this study, we produced a 50-year simulation using a revised version of CFSv2 (Huang et al., 2015), which was initialized from the Climate Forecast System Reanalysis (CFSR, Saha et al., 2010), initial conditions of atmosphere, land, sea ice, and ocean at 00Z, 1 January 1980 with a fixed greenhouse gas level for 2000 (Shukla et al., 2017). For the analysis, we have used the last 30 years of the 50-year simulation and compared the 30-year climatology of model simulation with the CFSR climatology derived from the same number of years (1979–2008).

In addition, we have used a set of 9-month ensemble reforecasts using the revised version of CFSv2 from initial conditions at the beginning of each month from January to May for the 30-year period of 1979–2008. All reforecasts are integrated to the end of September. To sample uncertainty in the ocean initial state, the ocean component was initialized with four different sets of ocean initial conditions: NCEP CFSR (Saha et al., 2010), NCEP Global Ocean Data Assimilation System (Behringer, 2005), European Centre for Medium-Range Weather Forecasts (ECMWF) Ocean Reanalysis System 3 (ORA-S3) (Balmaseda et al., 2008), and ECMWF Comprehensive Modeling of the Earth System for Better Climate Prediction and Projection (COMBINE-NV; Balmaseda et al., 2013). Four ensemble members were generated for each ocean initial condition using the instantaneous atmospheric and land surface initial conditions at 0000 UTC of the first 4 days from CFSR. The total number of ensemble members is 16 for each initial month. Although the reforecasts are initialized in every month from January to May, we will concentrate on the results from the February and May initialized reforecasts (FIR and MIR hereafter; see Shukla, Huang, Dirmeyer, Kinter, Shin, & Marx, 2019) as representative of the typical initial states for winter and late spring.

The monthly gridded surface temperature and subsurface soil temperature in four layers (0–10, 10–40, 40–100, and 100–200 cm) from CFSR are used for the period of 1979–2008 (Saha et al., 2010). We have also used monthly SWE (kg/m^2) from the Global Land Data Assimilation System, version 2.0, (GLDAS-2.0) for 2000–2016 at a resolution of 0.25° latitude by 0.25° longitude (Rodell et al., 2004). Radiation fluxes, SCF,

and surface albedo are available from the Clouds and the Earth's Radiant Energy System (Wielicki et al., 1996) Energy Balanced and Filled (CERES-EBAF) data set for the recent period (2001–2015) at 1° × 1° resolution. The surface sensible and latent heat flux data for 1979–2007 are converted from the European Centre for Medium-Range Forecasts Interim Re-Analysis (ERA-Interim; Dee et al., 2011) on the spectral resolution of T255. Gridded monthly temperature, wind (u, v), and geopotential height (H) at various levels from CFSR are also used. We have employed monthly means based on the instantaneous prognostic fields at 00Z in both the CFSv2 simulation and reanalysis.

For quantitative model-data comparison, both model and observational fields are interpolated onto a common 1° × 1° grid. We have tested the statistical significance of the bias (i.e., model minus reanalysis) patterns by a pointwise Student's t test. The biases discussed in this paper are statistically significant above the 99% confidence level at most of the centers of action.

3. Mean State and Biases During Spring and Summer Season in CFSv2 Simulation

In this section, we discuss the characteristic features of LST (obtained by masking out ocean points from skin temperature model output), rainfall, 850 hPa-winds, H850 and SUBT at 0–10 cm and 100–200 cm over North America (NA) during spring and summer in the simulation. Figure 1 shows the seasonal mean LST in CFSR (Figure 1a) and CFSv2 simulation (Figure 1b) for March–May mean (MAM). The corresponding model biases (CFSv2 minus CFSR) are given in Figure 1c. Qualitatively, the model captures the main spatial distribution of the reanalysis LST pattern, including colder temperature to the northeast region (NER; hereafter) between 55°N to 75°N and warmer temperature in the southwest region between 15°N and 35°N. The model also captures the LST gradient between the southwest and northeast regions. Quantitatively, the model depicts large cold bias of 5–9 °C in NER mainly between 44°N and 58°N, 85°W and 62°W (outlined by the green box in Figure 1c that include Maine, northern region of New York, Vermont, New Hampshire and Ontario, Quebec, central eastern Canada). CFSv2 also simulates spatial distribution of SCF in the northern region reasonably well (Figures 1d and 1e) but overestimates SCF up to 40% to 60% over NER, mainly between 45°N and 60°N (Figure 1f). Consistent with the bias of SCF, the model simulation depicts large positive bias in surface albedo (SA) ranging from 0.25 to 0.40 over NER (Figure 1i).

Due to the large cold bias near the surface over NER (Figure 1c), the model underestimates the 850 hPa geopotential heights (H850; Figure S1c in the supporting information) for 20–30 gpm over NER and in the northern Atlantic between 45°N and 60°N during MAM, where the model depicts large cold SST bias (not shown). Because of geostrophic balance between wind and geopotential height gradient, the large bias in H850 in turn contributes to a positive bias in 850 hPa winds of 1.2–2.4 m/s over NER (Figure S1f). The location of the wet rainfall bias (Figure S1i) over the central Great Plains is located southward in comparison to lager positive bias in lower level (850 hPa, Figure S1f) and middle-to-upper level (500 and 200 hPa; not shown) westerly winds.

The CFSv2 simulation (Figures 2b, 2e, and 2h) captures the main spatial distribution of reanalysis (Figures 2a, 2d, and 2g) LST and SUBT (0–10 and 100–200 cm) patterns over NA, including the LST gradient between northern and southern regions in the seasonal mean of July–September (JAS). The model demonstrates a large cold LST bias up to 9 °C over the central Great Plains between 35°N and 48°N, 108°W and 88°W (outlined by the red box in Figure 2c that include Minnesota, Iowa, Missouri, Nebraska, North Dakota, South Dakota, and eastern portion of Montana, Wyoming, Colorado, Kansas and northern portion of New Mexico, Oklahoma, Arkansas). Consistent with this cold bias of LST, the model also depicts large cold bias in SUBTs at 0–10 cm (Figure 2f) and 100–200 cm (Figure 2i) over the central Great Plains up to 9 °C. On the other hand, the model shows a cold bias at deep soil layer (100–200 cm) up to 2–5 °C over NER and the magnitude of its LST cold bias is less (~0.5 to 1 °C) there. It is noticeable that model simulation depicts less bias in LST and upper soil temperature in comparison to the deep soil temperature bias in NER.

The model demonstrates a wet rainfall bias over the central Great Plains up to 1.8 mm/day during July–September (Figure S2i). The centers of the large wet rainfall bias and large cold bias are both over the central Great Plains. This is also the region where cold biases from SUBTs at 0–10 to 100–200 cm are large. The model also depicts large negative bias of surface sensible heat flux (SSHF; Figure S3b) about 25 W/m^2 over the central Great Plains during summer due to large cold bias. The magnitude of positive bias of surface

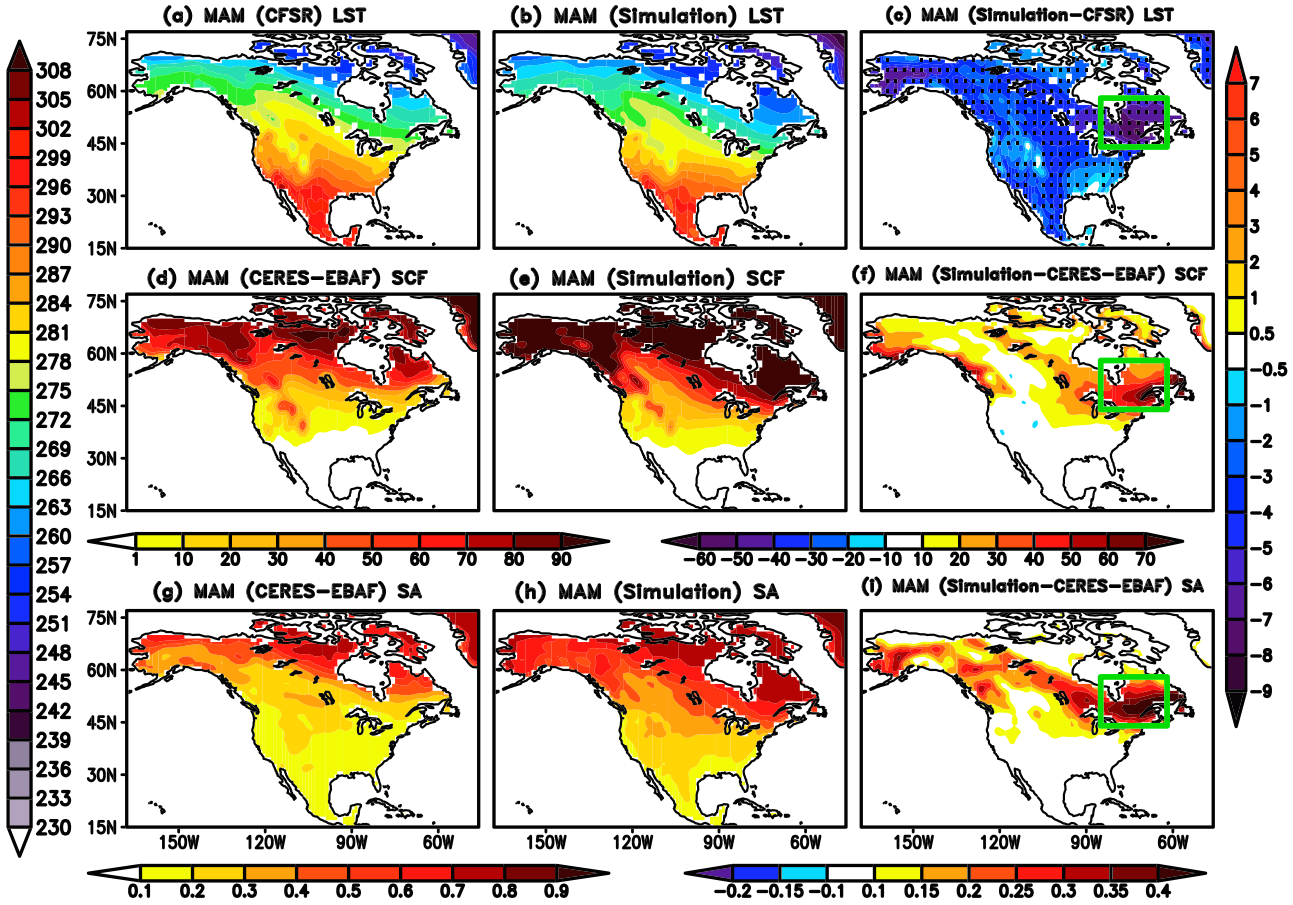

Figure 1. Spatial distributions of the climatological seasonal mean MAM LST (°K) in (a) CFSR, (b) CFSv2 simulation, and (c) climatological LST biases relative to CFSR over the North America continent. The scale for the magnitude for climatology (bias) of LST is shown at the left (right) of these panels. (d and e) As in (a) and (b) but for MAM SCF. (f) As in (c) but for MAM SCF bias. The scale for the magnitude for climatology (bias) of SCF is shown below these panels. (g and h) As in (a) and (b) but for MAM surface albedo (SA). (i) As in (c) but for MAM SA bias. The scale for the magnitude for climatology (bias) of SA is shown below these panels. The dotted regions indicate the statistically significant at 99% confidence level based on a Student's *t* test in (c).

latent heat flux (SLHF; Figure S3d) is about 25 W/m^2 over the Central Great Plains. The ratio between sensible and latent heat fluxes over the central Great Plains is much less than one in simulation, which indicates moist surface during summer. We have also found underestimate of SSHF and overestimate of SLHF over the central Great Plains in FIR, MIR (not shown), and also in the CFSRR February and May (Saha et al., 2014; http://cfs.ncep.noaa.gov) initialized reforecasts (not shown). We will discuss in detail the influence of SUBT on the LST in different subregions of NA during summer in section 5.

4. Sensitivity of Spring and Summer Simulation to Initial Conditions

We will now discuss how the magnitudes and spatial structures of bias in LST, SCF, SA, and SUBT at four layers vary in the simulation, FIR and MIR. Qualitatively, the simulation (Figure 3b) and FIR (Figure 3d) are able to reproduce reanalysis (Figure 3a) LST gradient between the northeast (mainly between 55°N and 75°N) and southwest (mainly between 35°N and 50°N) regions in March. Quantitatively, the simulation depicts large cold bias of 7–9 °C (Figure 3c) over NER although the magnitude of cold bias in FIR (Figure 3e) is smaller (2–3 °C) there. The difference of the cold bias magnitudes in the simulation and the reforecasts suggests that the bias starts to grow from the initial states and may take several years to be saturated. In June, the simulation depicts cold LST bias up to 5 °C (Figure 3h) over the central Great Plain although the magnitude of the corresponding cold bias in FIR (up to 2 °C; Figure 3j) and MIR (up to 0.5 °C; Figure 3l) is much less. FIR (Figure 3j) depicts warm bias by 1–2 °C in June over most of the northern

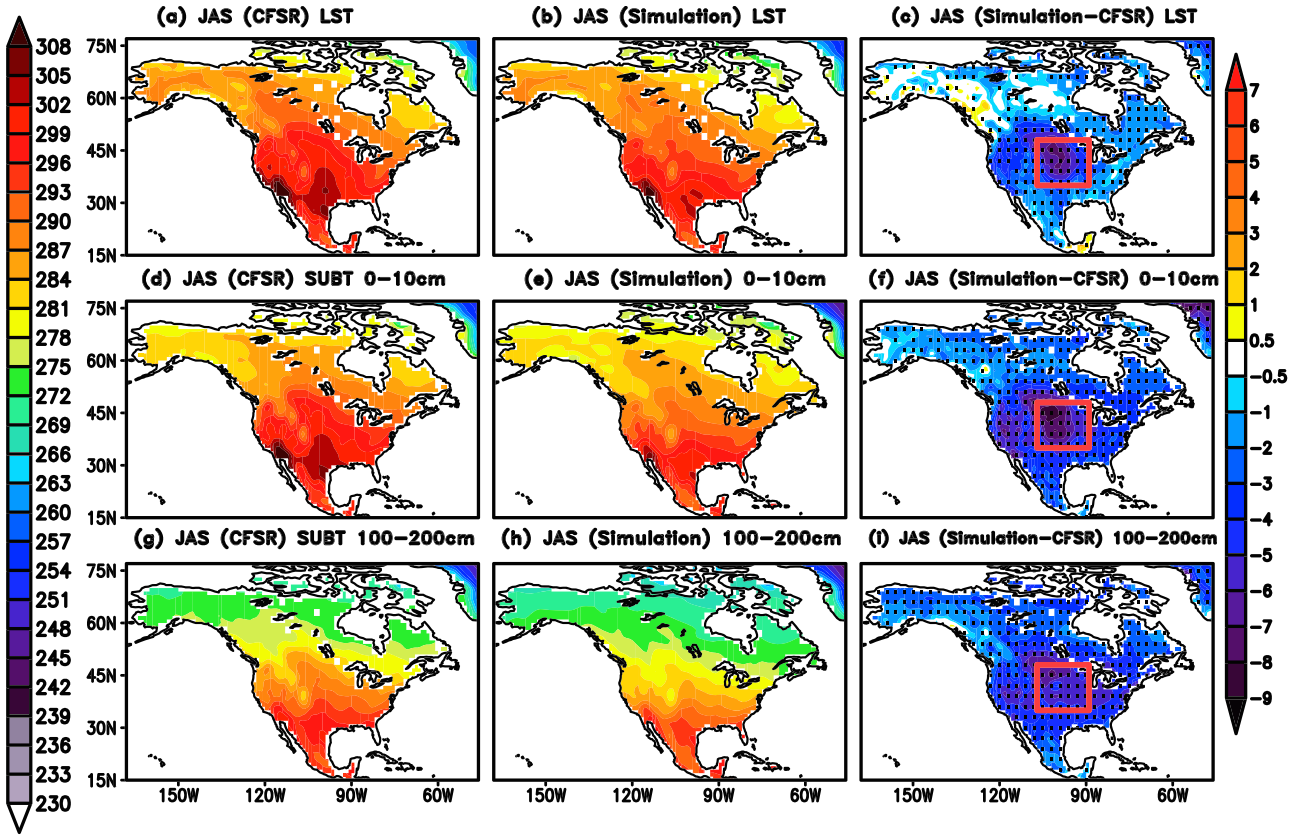

Figure 2. Spatial distributions of climatological seasonal mean JAS LST (°K) in (a) CFSR, (b) CFSv2 simulation, and (c) climatological LST biases relative to CFSR over the North America continent. The scale for the magnitude for climatology (bias) of LST is shown at the left (right) of these panels. (d)–(f) As in (a)–(c) but for JAS subsurface soil temperature (SUBT) at 0–10 cm. (g)–(i) As in (a)–(c) but for JAS SUBT at 100–200 cm. The dotted regions in bias map indicate the statistically significant at 99% confidence level based on a Student's *t* test.

Pacific, Alaska, and western Canada. MIR (Figure 3l) depicts even larger warm bias (up to 7 °C) in these areas, as well as the western United States. From early spring to early summer, a cold bias prevails in LST over NER in the simulation. However, the magnitude of the cold bias is smaller in June (Figure 3h) than in March (Figure 3c).

To examine the roles played by the snow properties in sustaining the LST bias, first we examine SCF and SA over the NA region. Based on CERES-EBAF and GLDAS-2.0 products (Figure S4), the establishments of the stable snow cover over NA region occurs in October over western coast of NA (Figure S4a) mainly between 60°N and 75°N and snowmelt starts in April. Qualitatively, the simulation captures the transition of snow properties (establishment and disappearance period of snow cover) over the NA region (not shown). Quantitatively, it overestimates SCF in October for up to 60% over NER between 65°N and 75°N (Figure 4a). During November and December, the simulation overestimates SCF for up to 70% between 45°N and 60°N, 90°W and 75°W (Figures 4b and 4c). The dominant center of SCF biases also shifts southeastward from October to December. For example, the location of maximum SCF bias in NER shifts from 57°N in November to 45°N in December. During the snow-melting season, the simulation depicts a positive SCF bias ranging from 50 to 70% over NER from April to June. During this period, FIR depicts less positive bias of SCF over NER (Figures 4i–4m). For example, FIR (Figure 4m) only overestimates SCF by 10–20% over NER in June while the simulation depicts a 30–50% overestimate there (Figure 4h). Furthermore, the SCF bias in MIR is negligible during June (Figure 4o) because the MIR integration does not pass the winter season. The model simulation (not shown) captures the development and transitions of SWE over the NA region as the reanalysis (Figure S4i–S4p) does but overestimates the SWE amount over NER from October to subsequent June (Figure S5). The magnitude of SWE bias in the simulation is larger than that in FIR

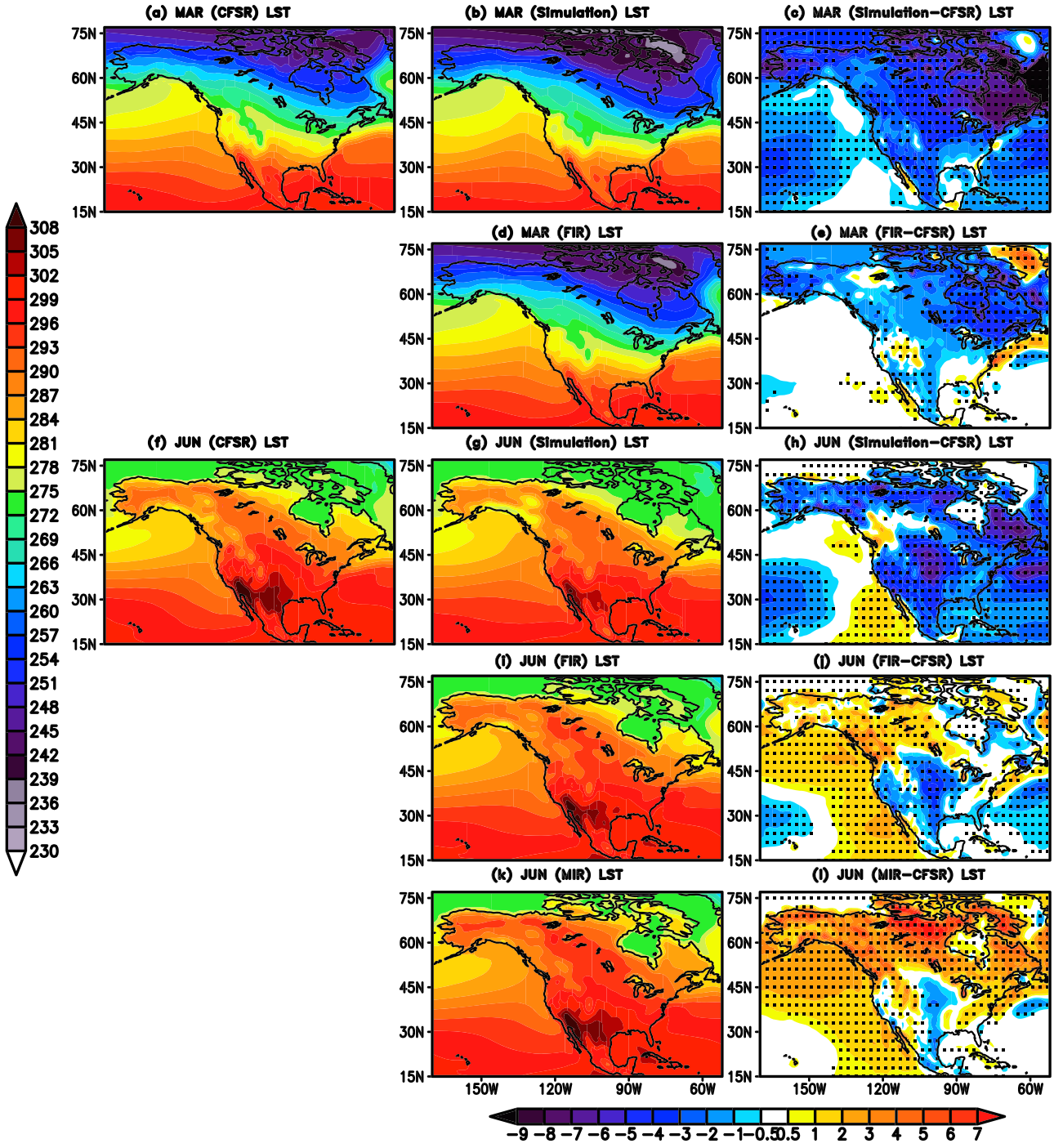

Figure 3. Spatial distributions of March climatology of LST in (a) CFSR, (b) CFSv2 simulation, and (c) climatological march LST biases relative to CFSR over the North America. The scale for the magnitude for climatology (bias) of LST is shown at the left (below) of these panels. (d) and (e) As in (b) and (c) but for MAR FIR. (f)–(h) As in (a)–(c) but for June climatology of LST in model simulation. (i) and (j) As in (g) and (h) but for Jun FIR. (k) and (l) As in (g) and (h) but for Jun MIR. The dotted regions in bias map indicate the statistically significant at 99% confidence level based on a Student's *t* test.

(Figure S5). Consistent with the biases of SCF and SWE, the simulation also depicts large positive SA bias in NER for up to 0.4 (Figure S6a–S6h) and FIR (Figure S6i–S6m) for up to 0.25.

It is found that the pattern of the SCF simulation bias relative to CFSR is similar to that relative to CERES-EBAF and, as expected, the magnitude of SCF bias is slightly lower in the former than in the

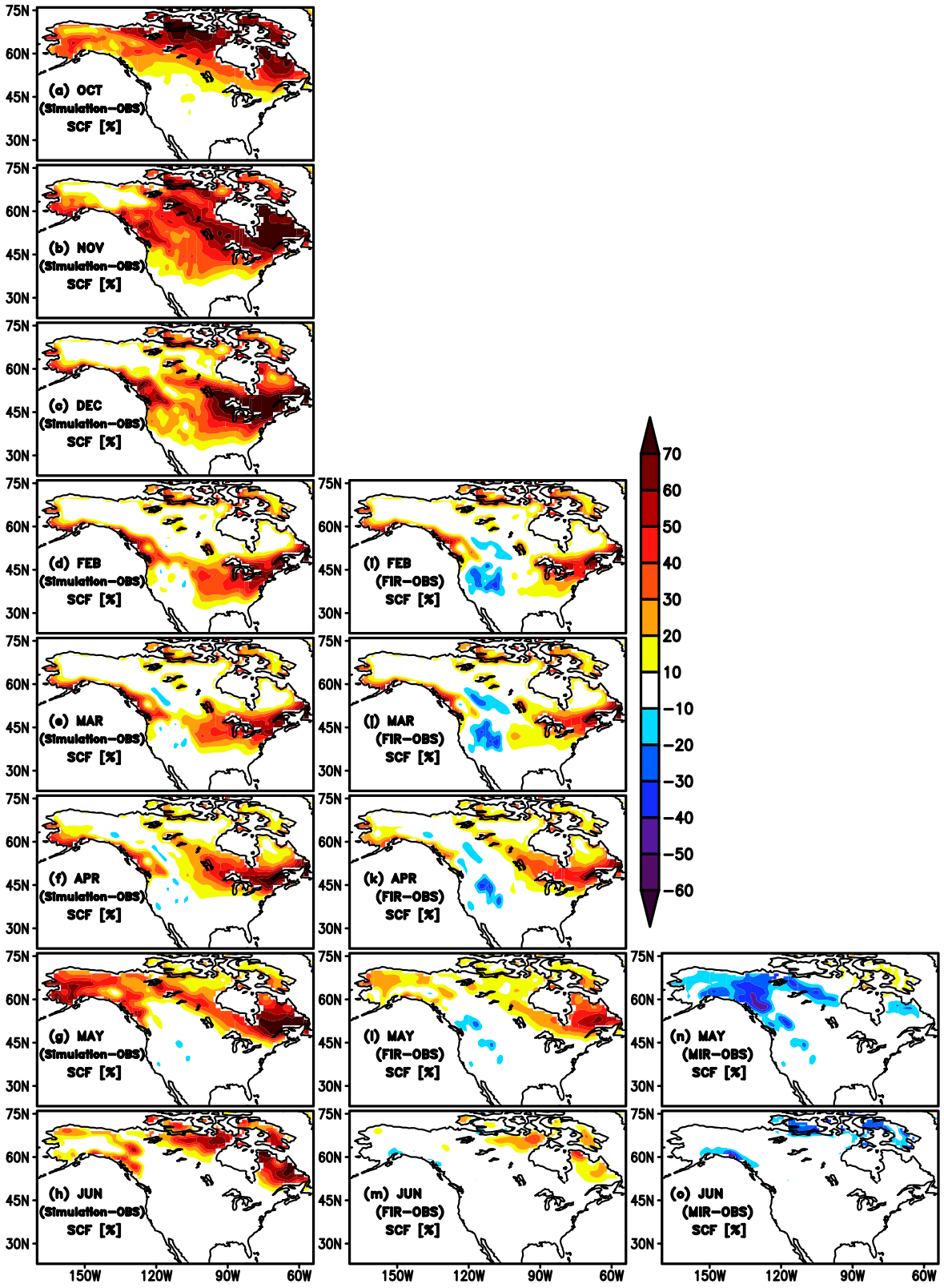

Figure 4. Spatial distributions of monthly snow cover fraction (SCF; %) climatological biases relative to CERES-EBAF SCF (OBS) in CFSv2 simulation for (a) October, (b) November, (c) December, (d) February, (e) March, (f) April, (g) May, and (h) June over the North America continent. Monthly SCF climatological biases relative to CERES-EBAF SCF in FIR for (i) February, (j) March, (k) April, (l) May, and (m) June. Monthly SCF climatological biases relative to CERES-EBAF SCF in MIR for (n) May and (o) June.

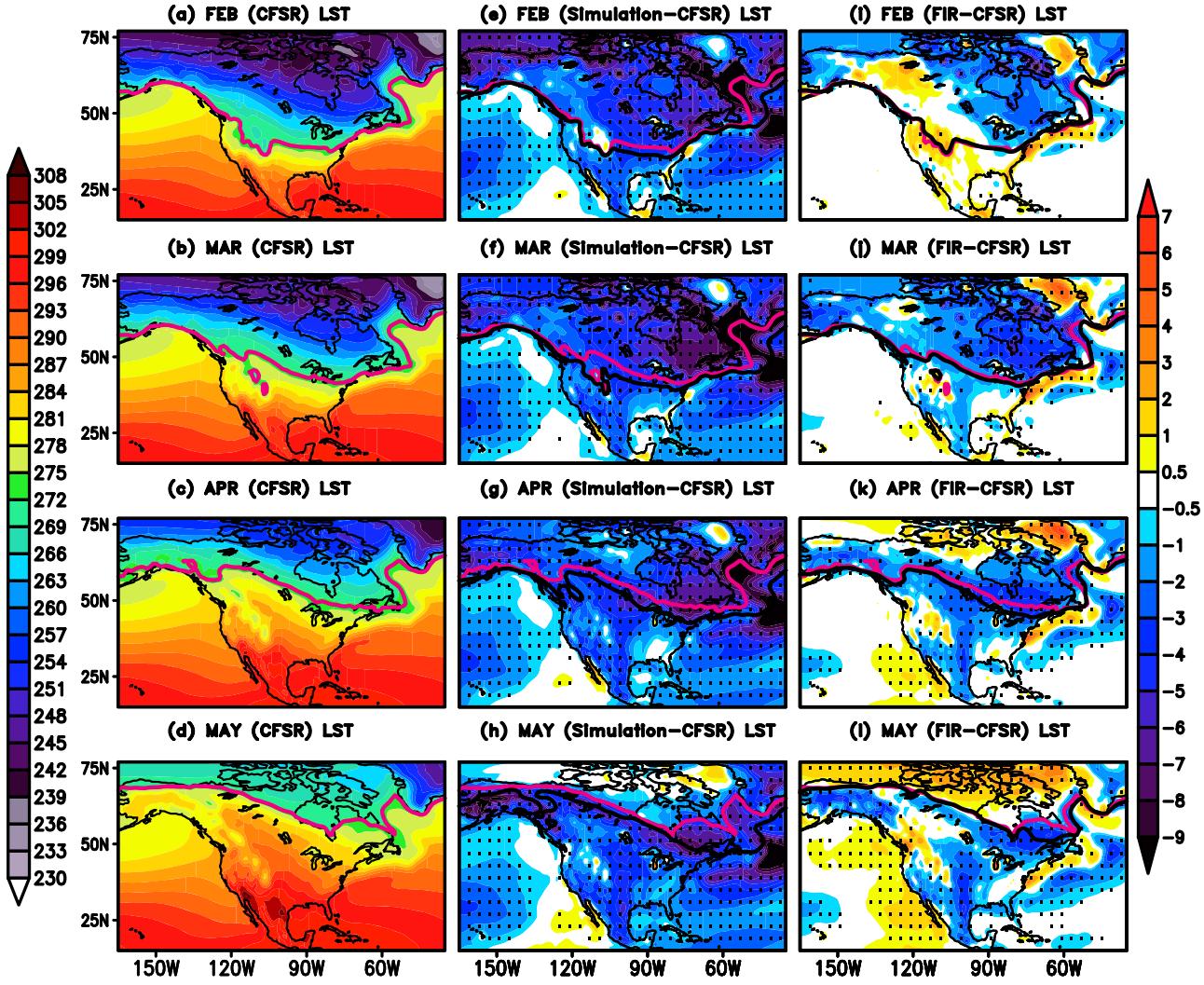

Figure 5. Spatial distribution of monthly climatological CFSR LST (^{O}K) in (a) February, (b) March, (c) April, and (d) May over the North America. The scale for the magnitude for LST in °K is shown at the left of these panels. Spatial distributions of the monthly climatological LST bias relative to CFSR in model simulation for (e) February, (f) March, (g) April, and (h) May. The scale for the magnitude of bias for LST in °K is shown at the right of these panels. Both red and black lines in all the panels depict 273.15 °K (freezing temperature) for CFSR (red line) and model simulation (black line). (i)–(l) As in (e)–(h) but for FIR. The dotted regions indicate the statistically significant at 99% confidence level based on a Student's *t* test in (e-l).

latter. It is also notable that FIR depicts negligible bias in the first month of reforecasts because the CFSv2 model is initialized with CFSR initial conditions. From April to June, the structure of the SCF bias in FIR and the simulation relative to CFSR is similar to each other but the former is still somewhat weaker in magnitude throughout the reforecasts (not shown).

Overall, the model simulation overestimates SCF, SWE, and SA during early winter (November–December) and from midspring to early summer (April–June) over NER where large cold LST bias also exists in these seasons. What is the possible cause of slow and delay snow melting over the NER of NA during April–June in simulation in comparison to FIR? To explore the cause for delayed snow melting over the NER in the simulation, we have displayed monthly climatological bias of LST in the simulation (Figures 5e–5h) and FIR (Figures 5i–5l) from February to May. It should be noticed that, in addition to the LST bias, the contour of the freezing temperature (273.15 °K) is a good indicator of the sustainable snow on the ground. The locations of the freezing temperature are shown for CFSR (red line; Figures 5a–5d), the simulation (black line; Figure 5e–5h) and FIR (black line; Figures 5i–5l). The cold LST bias in the simulation is larger than in FIR over NER from February to May. The cold SST bias in the northern Atlantic Ocean (AO) is larger

in simulation (Figures 5f–5h) than FIR (Figures 5j–5l) during March to May. It is necessary to mention that the freezing temperature in both CFSR and FIR is located at almost identical location during February and March over NER (Figures 5i–5j) whereas a discrepancy in location of freezing temperature line between the simulation and CFSR (Figures 5e–5f) is found over the northern AO. In the simulation, the location of freezing temperature is northeastward mainly over the northern AO between 50°N and 60°N, whereas its location is close to CFSR over land. We have reconfirmed this bias in the location of freezing temperature over the northern AO using the NOAA OISST v2 and the simulated SST (Figures S7m–S7p) from February to May, as well as in comparison to FIR (Figures S7q–S7t). A drastic change in the location of freezing temperature in CFSR is observed during May when it moves quickly northward over NER in comparison to its location in March due to response to solar heating (Figure 5d). Its location in FIR (Figure 5i) is slightly southward in comparison to CFSR in May (Figure 5d) and difference in location between CFSR and FIR is the region where FIR overestimates SCF during May. On the other hand, we found large disagreement in the location of freezing temperature contour between the simulation (Figures 5g–5h and Figures S7o and S7p) and CFSR (Figures 5c and 5d and Figures S7g and S7h) during April and May over NER. It is found that the freezing temperature contour in simulation is still over the northern AO. This may be an important cause for larger biases in snow properties over NER in the simulation than in FIR.

Why does CFSv2 produce early and fast growth of SCF over NER from October to December in simulation? To explore the possible causes for early and fast increase of SCF over NER in the simulation, we display monthly climatological LST in CFSR (Figures 6a–6e) and the corresponding model biases (Figures 6f–6j) during July–November. The model simulation reproduces the main features of the CFSR LST during these months but underestimates the LST by 4 to 9 °C (Figures 6f–6j) except in Alaska and western central Canada in July and August (Figures 6f and 6g). The locations of freezing temperature contours in CFSR (red line) and the simulation (black line) are almost identical over the northern region during July and August (Figures 6f and 6g). In September, the location of the freezing line in simulation is located slightly more southward than in CFSR (Figure 6h). A dramatic feature is found during October in the simulation (Figure 6i) when the model's freezing line moves quickly southward in NER from 67°N in September to near 50°N. The location of CFSR's freezing line is northward to its location in the simulation. It is necessary to note that the southward shift in the location of freezing line in the simulation during October and November is just over land (Figures 6i and 6j). Since LST reaches the freezing point earlier over NER in the simulation than in CFSR, new snow falling on the frozen ground cannot melt and starts to accumulate in the model. These results suggest that the positive snow-albedo feedback starts earlier in the model simulation than in nature over the NER of NA (see Shukla, Huang, Dirmeyer, & Kinter, 2019 for similar features over the western Eurasia). Therefore, the simulation overestimates SCF in early winter and probably total snow amount throughout the winter. This leads to the prolonged melting processes in late spring and early summer. This scenario easily explains the differences among FIR, MIR, and the simulation because FIR does not experience the early startup of the snow-albedo feedback in the previous fall as the simulation does. Starting from May, MIR is not affected by the model snow-albedo feedback process at all.

5. Influence of Subsurface Soil Temperature on the LST

In this section, we discuss the cumulative influence of SUBT on LST over different subregions of the NA continent, and a possible relationship between net surface heat flux and SUBT. We first discuss the monthly climatology of SUBT at all layers in CFSR (Figures S8a–S8l) and simulation, and then the corresponding model biases (CFSv2 minus CFSR; Figures 7a–7l). A strong meridional gradient of SUBT at all layers between southern and northern regions of NA is found in CFSR during July–September (Figure S8a–S8l). The simulation reproduces this gradient at all layers qualitatively (not shown). The locations of freezing temperature line in monthly climatological variations of SUBT at 0–10 and 10–40 cm (Figures S8a–S8f; red line) are almost the same as in LST (Figures 6a–6c) over northern region of NA in CFSR. The model simulation also reproduces qualitatively the locations of freezing temperature line at 0–10 and 10–40 cm (Figures S8a–S8f; black line). A northeastward shift in freezing temperature at 100–200 cm from July to September is found in CFSR (Figures S8j–S8l; red line), whereas its location in simulation at deep soil layer (Figures S8j–S8l; black line) is always southward in comparison to CFSR. The spatial structure and magnitude of the SUBT cold bias at 0–10 cm (Figures S9e and S9f) and 10–40 cm (Figures S9h and S9i) during May–June over NER are similar to the LST bias there (Figures S9b and S9c). During April and May, the model depicts

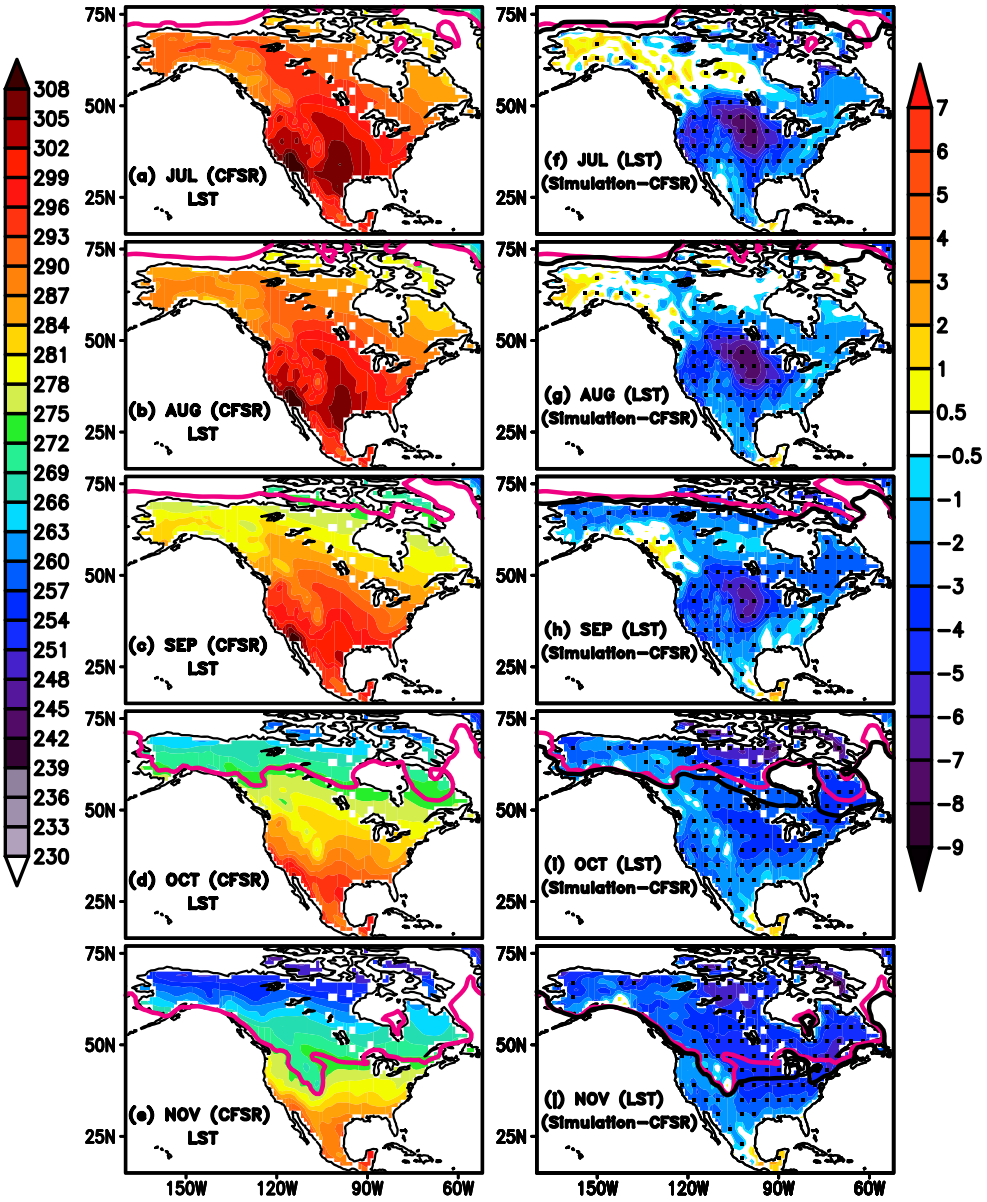

Figure 6. Spatial distribution of monthly climatological CFSR LST (°K) in (a) Jul, (b) August, (c) September, (d) October, and (e) November over the North America continent. The scale for the magnitude for LST in °K is shown at the left of these panels. Spatial distributions of the monthly climatological LST bias relative to CFSR in model simulation for (f) July, (g) August, (h) September, (i) October, and (j) November. The scale for the magnitude of bias for LST in °K is shown at the right of these panels. Both red and black lines in all the panels depict 273.15 °K (freezing temperature) for CFSR (red line) and model simulation (black line). The dotted regions indicate the statistically significant at 99% confidence level based on a Student's *t* test in (f)–(j).

warm bias at deep soil layer over the northern region (Figures S9m and S9n). The magnitude of cold biases at upper soil layer in June (Figure S9f) over NER is larger in comparison to deep soil layer (Figure S9o). The large cold bias in upper soil layer in June is related to the large cold LST bias due to the overestimated SCF.

During July–September, the SUBT at 100–200 cm has a noticeably smaller seasonal change in the model simulation in comparison to CFSR, resulting in a large cold bias during summer up to 4–6 °C over most of the North America continent (Figures 7j–7l), although its winter SUBT at 100–200 cm is realistic. The influence of cold bias of SUBT from deep to upper soil layers on LST is different over the subregions of NA continent (e.g., the central Great Plains, the western USA and the NER of NA). The simulation depicts large cold bias of SUBT at 0–10 cm up to 9 °C over the central Great Plains (Figure 7a, outlined by red box).

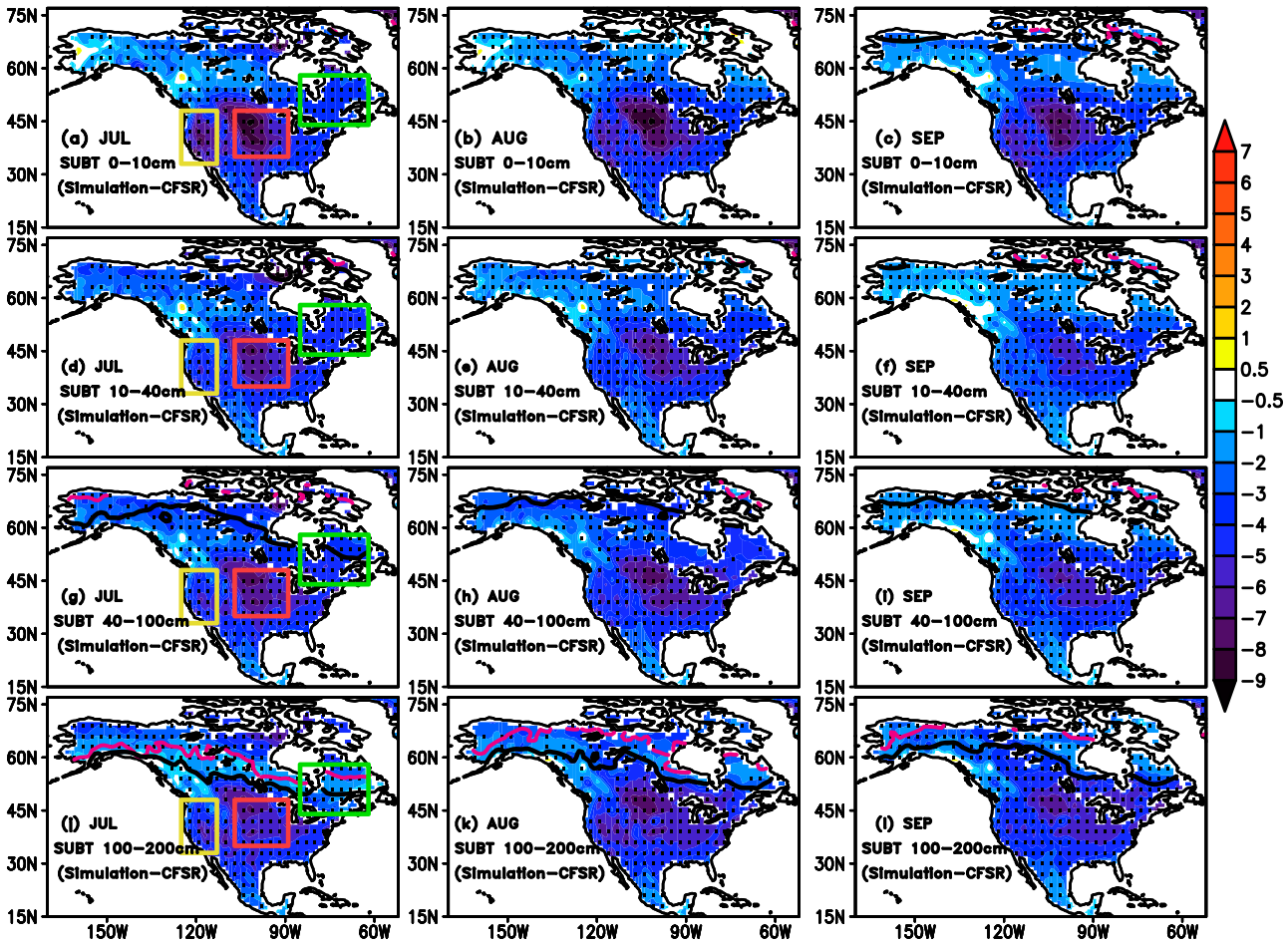

Figure 7. Spatial distributions of monthly SUBT at 0–10 cm climatological biases relative to CFSR in CFSv2 simulation for (a) July, (b) August, and (c) September over the North America continent. The scale for magnitude for SUBT bias in °K is shown at the right of these panels. The red line (black line) denotes 273.15 °K in CFSR (model simulation) SUBT at 0–10 cm. (d)–(f) As in (a)–(c) but for SUBT at 10–40 cm. (g)–(i) As in (a)–(c) but for SUBT at 40–100 cm. (j)–(l) As in (a)–(c) but for SUBT at 100–200 cm. The dotted regions indicate the statistically significant at 99% confidence level based on a Student's *t* test.

The magnitude of this cold bias is similar from upper to deep soil layer (100–200 cm) from July to September. To explore the cause of the LST cold biases (Figure 2c), Figure 8 shows the area-averaged climatological LST and SUBT at four layers over the central Great Plains in CFSR, the simulation, FIR and MIR (Figures 8a, 8c, and 8e). The corresponding differences (model-CFSR) are also displayed in Figures 8b, 8d, and 8f, respectively. Qualitatively, the model is able to capture the evolution of LST and SUBT in simulation and reforecasts. Quantitatively, the model depicts cold bias up to 6.0 °C at all the SUBT layers from upper to deep soil layers from July to September. During winter season, the simulation depicts warm bias up to 1.0 °C at 10–40 cm (green line, Figure 8b), 40–100 cm (red line, Figure 8b), and 100–200 cm (blue line, Figure 8b), whereas a cold bias up to 2.0 °C is found for SUBT at 0–10 cm (black line, Figure 8b). The magnitude of LST bias (purple line, Figure 8b) is less in comparison to SUBT biases from July to September. In the reforecasts, the model bias is generally small in the first month of integration and grows as the forecast month increases. Furthermore, we have found that, although the magnitude of LST is nearly equal to the SUBT bias at all layers in February in FIR, the magnitude of cold SUBT bias during July–September is larger (up to 5.0 °C) than the LST bias (up to 2.5 °C) (Figure 8d). Therefore, the rate of increase of cold SUBT bias at all layers from February to September in FIR is larger than the increase rate of the cold LST bias. This increase of cold SUBT and LST biases is also found in MIR (Figure 8f) from May to September. From July to September, CFSv2 also depicts wet bias in the central Great Plains in both simulation and FIR. MIR also depicts wet rainfall bias over the central Great Plains but its

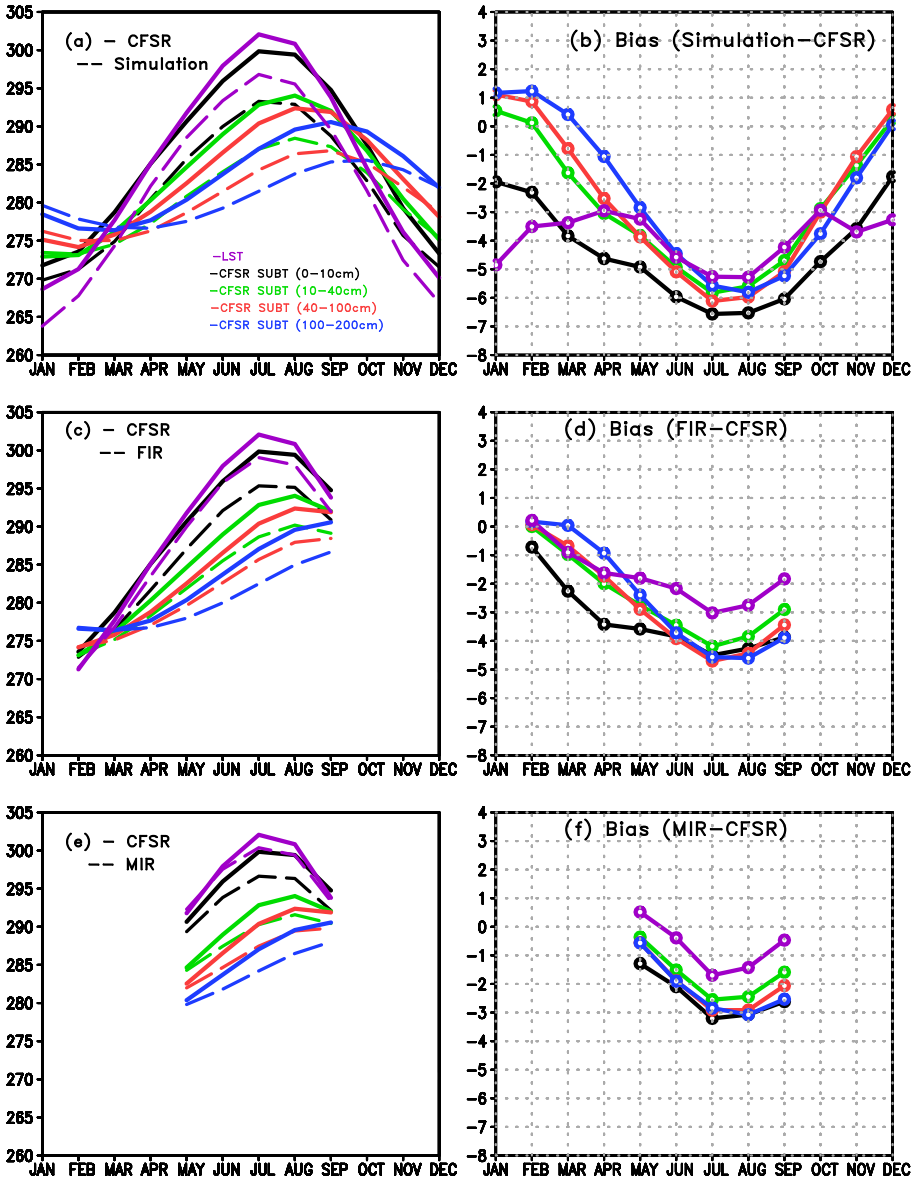

Figure 8. (a) The area averaged monthly climatological SUBT over the central Great Plains (outlined by the red box in Figure 7; 35-48°N, 253–271°E) at 0–10 cm (black line), 10–40 cm (green line), 40–100 cm (red), 100–200 cm (blue), and LST (purple line). The solid line indicates the CFSR and long dashed line indicates the CFSv2 simulation. (b) The area average of climatological bias between CFSv2 and CFSR over the (CFSv2-CFSR) for 0–10 cm (black line), 10–40 cm (green line), 40–100 cm (red line), 100–200 cm (blue line), and LST (purple line). (c) As in (a) but for FIR. (d) As in (b) but for FIR. (e) As in (a) but for MIR. (f) As in (b) for MIR.

magnitude is less than in the simulation and FIR (not shown). We may conclude that severe cold bias from upper (0–10 cm) to deep soil layer (100–200 cm) over the central Great Plains in model is one of the possible causes for large cold bias during July–September in both the simulation and reforecasts. As a result, the ratio between sensible and latent heat fluxes is much less than the one in simulation during summer. The latter may also contribute to an excessive summer rainfall over the central Great Plains.

The magnitude of cold bias from July to September at upper soil layer (0–10 cm; Figures 7a–7c) over NER (outlined by green box in Figure 7) is much smaller than the cold bias in previous May and June (Figures S9e and S9f). The cause of less cold bias in upper soil layer during summer may also be related to less cold LST bias because of the response to the solar heating. Quantitatively, the model simulation depicts large cold LST bias up to 5 to 6 °C during February to May over the NER but less cold bias up to 2 °C during July to September over the NER (purple line, Figure 9b). Model simulation depicts large cold bias up to

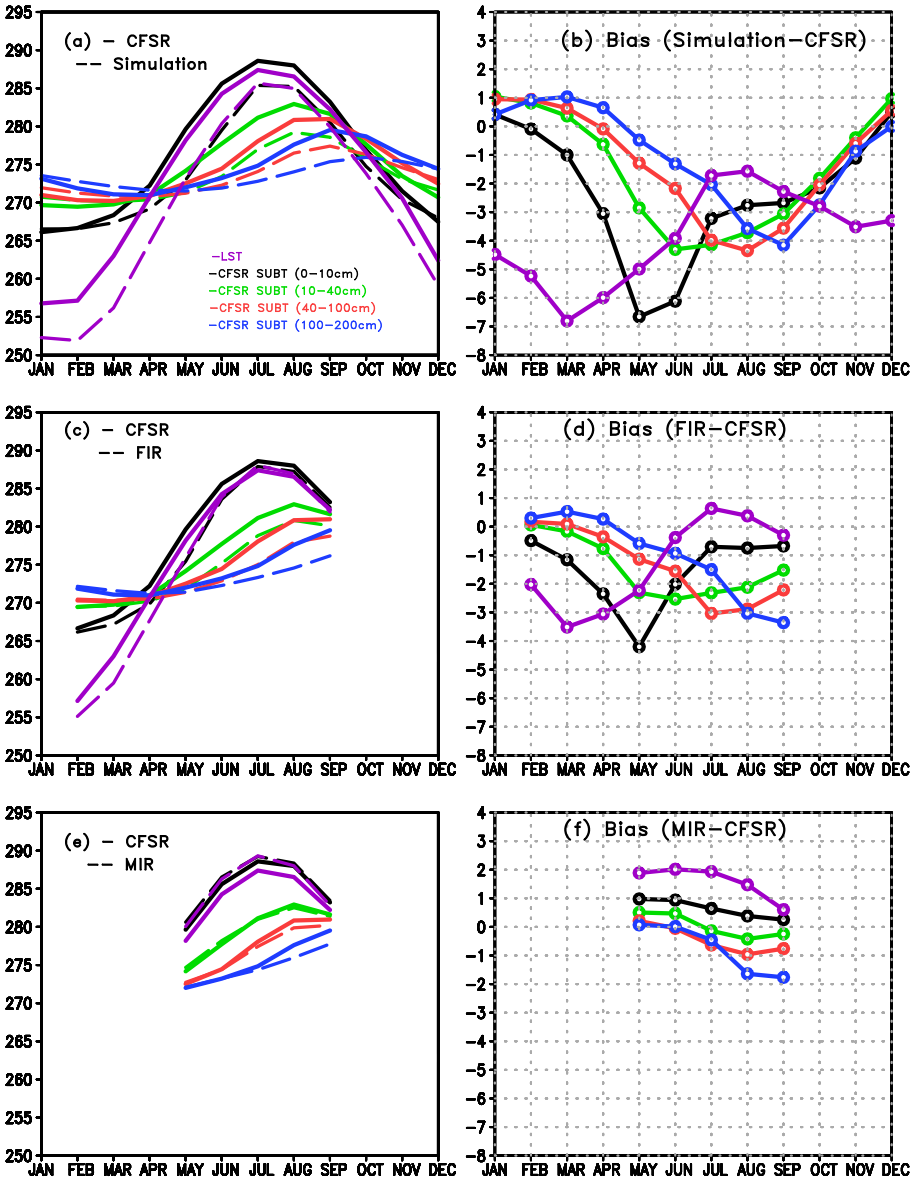

Figure 9. (a) The area averaged monthly climatological SUBT over the northeast region of North America (outlined by the green box in Figure 7; 44-58°N, 275–298°E) at 0–10 cm (black line), 10–40 cm (green line), 40–100 cm (red), 100–200 cm (blue), and LST (purple line). The solid line indicates the CFSR and long dashed line indicates the CFSv2 simulation. (b) The area average of climatological bias between CFSv2 and CFSR over the (CFSv2-CFSR) for 0–10 cm (black line), 10–40 cm (green line), 40–100 cm (red line), 100–200 cm (blue line), and LST (purple line). (c) As in (a) but for FIR. (d) As in (b) but for FIR. (e) As in (a) but for MIR. (f) As in (b) but for MIR.

6.5 °C at upper soil layer during May to June but less cold bias up to 2.7 °C during August to September (black line, Figure 9b), whereas model deep soil layer depicts warm bias up to 1.0 °C over the NER during February to April but large cold bias up to 4.0 °C during August to September (blue line, Figure 9b). The magnitude of cold deep soil temperature bias over the NER is larger in comparison to the upper one during August and September in simulation (Figure 9b). The difference in cold bias between deep soil layer and upper soil layer is larger in FIR (Figure 9d) in comparison to simulation (Figure 9b). Consistent with our results over western Eurasia in CFSv2 simulation (Shukla, Huang, Dirmeyer, & Kinter, 2019), it is found that when the solar radiation reduces quickly in the early fall, the cold SUBT bias at 100–200 cm in the NER during August–September causes additional cooling to the upper soil layer and helps to bring LST to the freezing point early in model simulation, which provides a favorable condition for excessive

SCF (Figures 4a–4c) in the subsequent October to November. Therefore, the intensity of deep soil temperature bias is a factor in determining the magnitude of the LST bias. To further explore the impact of late summer SUBT at 100–200 cm on early winter condition, we have selected five anomalous cold and warm years based on normalized interannual time series of SUBT at 100–200 cm during mean of July to September (JAS) over the NER in simulation. Figure S10a displays the difference between composite of cold and warm year SUBT at 100–200 cm during JAS, it depicts cooling over the NER. The composite analysis of SUBT 0–10 cm (Figure S10b) and LST (Figure S10c) also depict cooling in the following October. The simulated freezing temperature line during October in the cold years is located southwestward than its location in the warm years at SUBT 0–10 cm and LST. There is also a positive difference in SCF over there between cold and warm years (Figure S10d). Using the same analysis on CFSR does not show the same relationship (Figures S10e–S10h).

The oceanic influence may be dominant over western region of NA due to stronger upstream marine influence from the Pacific. This raises a question: Is there any impact of SUBT on LST over the western USA? To answer this question, the area average of climatological LST and SUBT over the western USA (outlined by the yellow box in Figure 7 that include California, Nevada, Oregon, and western portion of Washington and Idaho) is made in CFSR and model (Figures 10a, 10c, and 10e) and its corresponding differences are displayed in Figures 10b, 10d, and 10f. The magnitude of cold bias in simulation over the western United States is around 2 °C during January to December (Figure 10b, purple line), whereas model depicts large cold bias at all SUBT layers during June to August in comparison to LST bias. Model reforecasts also depicts large cold SUBT bias during summer in comparison to LST (Figures 10d and 10f). The magnitude of LST bias is almost same during winter, spring, and summer in simulation (around −2.0 °C; Figure 10b), FIR (around −0.4 °C; Figure 10d), and MIR (around 1.0 °C; Figure 10f). But, a sharp transition in the SUBT from upper to deep soil layer bias over the western United States is found during winter to summer in simulation and reforecasts. It may be possible that the impact of SUBT on LST over the western United States is negligible in simulation, FIR, and MIR due to stronger upstream marine influence from the Pacific.

To explore the relationship between surface net heat flux on subsurface transport between upper soil layer to deep soil layer, the climatological difference between SUBT at 100–200 cm and SUBT at 0–10 cm in CFSR is displayed in Figures 11a–11f) over the NA during May to October and corresponding model simulation biases (simulation minus reanalysis) are given in Figures 11g–11l. From May to September (Figures 11a–11e), heat is generally transferred downward within the soil over the NER because the deep soil layer is colder than the upper soil layer. The direction of heat transfer is revered in October (Figure 11f). In May (Figure 11g) and June (Figure 11h), the model depicts less cold gradient over the northeastern region; main cause for it is smaller temperature difference in simulation than that in CFSR because of delay in snow melting over the NER. From August to September, the model has negative temperature bias over there in simulation (Figures 11j and 11k), FIR (Figures S11d and S11e) and MIR (Figures S11i and S11j); one possible cause for it is the large negative downward temperature gradient in model than in CFSR. Therefore, from summer to early fall, the model upper soil layer loses more heat to deep soil layer in simulation than CFSR.

The climatological bias of net surface heat flux from May to October between the simulation and observations is shown in Figures 11m–11r as described in Shukla, Huang, Dirmeyer, Kinter, Shin, and Marx (2019) and Shukla, Huang, Dirmeyer, and Kinter (2019). The land surface is generally gaining more heat from the atmosphere in the simulation than in CFSR over NA from 35°N to 52°N during June–August. One possible cause is excessive solar radiation reaching the land surface due to inadequate cloud cover. This seems to compensate for the heat loss from the upper soil layer to the deep soil layer. As the net surface heat flux becomes negative in September at the same time when heat is transferred from the upper to deep soil layers, a rapid cooling of the upper soil layer is expected. During May and June, the model has a large negative bias of net energy over NER mainly between 55°N and 75°N, which may be related to the bias in surface SHF (Figures S12a and S12b) and net shortwave radiation (Figures S12m and S12n). The cause of net shortwave radiation bias is the excessive SCF and its SA over NER. The bias in surface SHF is mainly due to the large cold bias in LST over NER.

We have performed additional calculations using surface temperature from the Climatic Research Unit at the University of East Anglia (CRU 3.21; Harris et al., 2014). The CRU surface temperature data set is based on objective analysis of station observations and thus independent of model-based reanalysis products. One

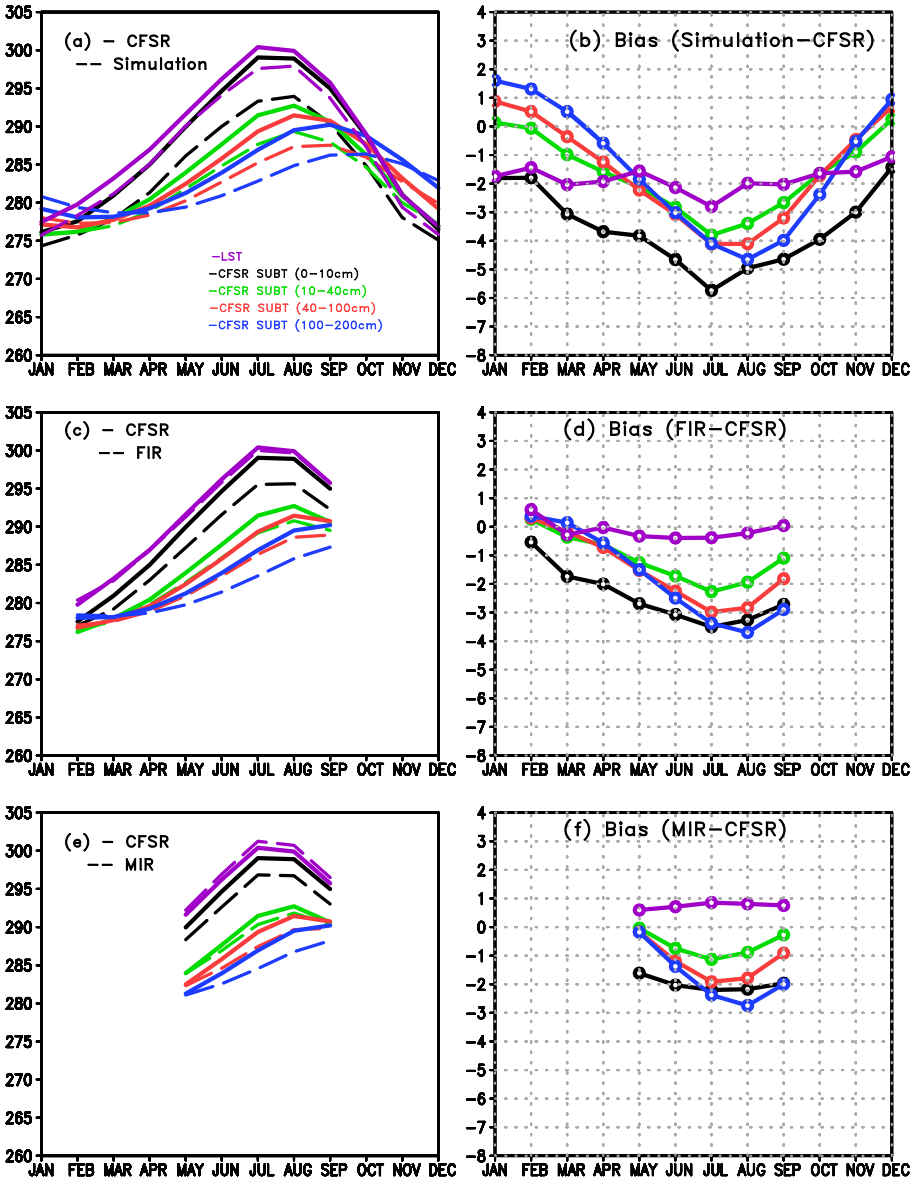

Figure 10. (a) The area averaged monthly climatological SUBT over the western America (outlined by the yellow box in Figure 7; 33-48°N, 235–247°E) at 0–10 cm (black line), 10–40 cm (green line), 40–100 cm (red), 100–200 cm (blue), and LST (purple line). The solid line indicates the CFSR, and the long dashed line indicates the CFSv2 simulation. (b) The area average of climatological bias between CFSv2 and CFSR over the (CFSv2-CFSR) for 0–10 cm (black line), 10–40 cm (green line), 40–100 cm (red line), 100–200 cm (blue line), and LST (purple line). (c) As in (a) but for FIR. (d) As in (b) but for FIR. (e) As in (a) but for MIR. (f) As in (b) but for MIR.

issue preventing us from making such comparison directly in the first place is the fact that our model output is the instantaneous field at 00Z while the station-based analyses are daily averages. As a result, the difference between the model output and the observations would be dominated by the diurnal change, that is, the difference between daily averages and the value at local time corresponding to 00Z. As an alternative, we had employed monthly means based on the instantaneous prognostic fields at 00Z in the CFSR (Saha et al., 2010) for the comparison. For this purpose, we have applied a three-step evaluation procedure to compare our model results with the station-based analysis indirectly. First, we calculated the bias of the monthly mean LST based on the *daily average* of 6-hourly instantaneous values (i.e., 00Z, 06Z, 12Z, and 18Z) in the NCEP CFSv2 Reanalysis and Reforecast (CFSRR) FIR (Saha et al., 2014; http://cfs.ncep.noaa.gov) with respect to the surface temperature from CRU 3.21 (Figure sS13a–S13f) over the NA

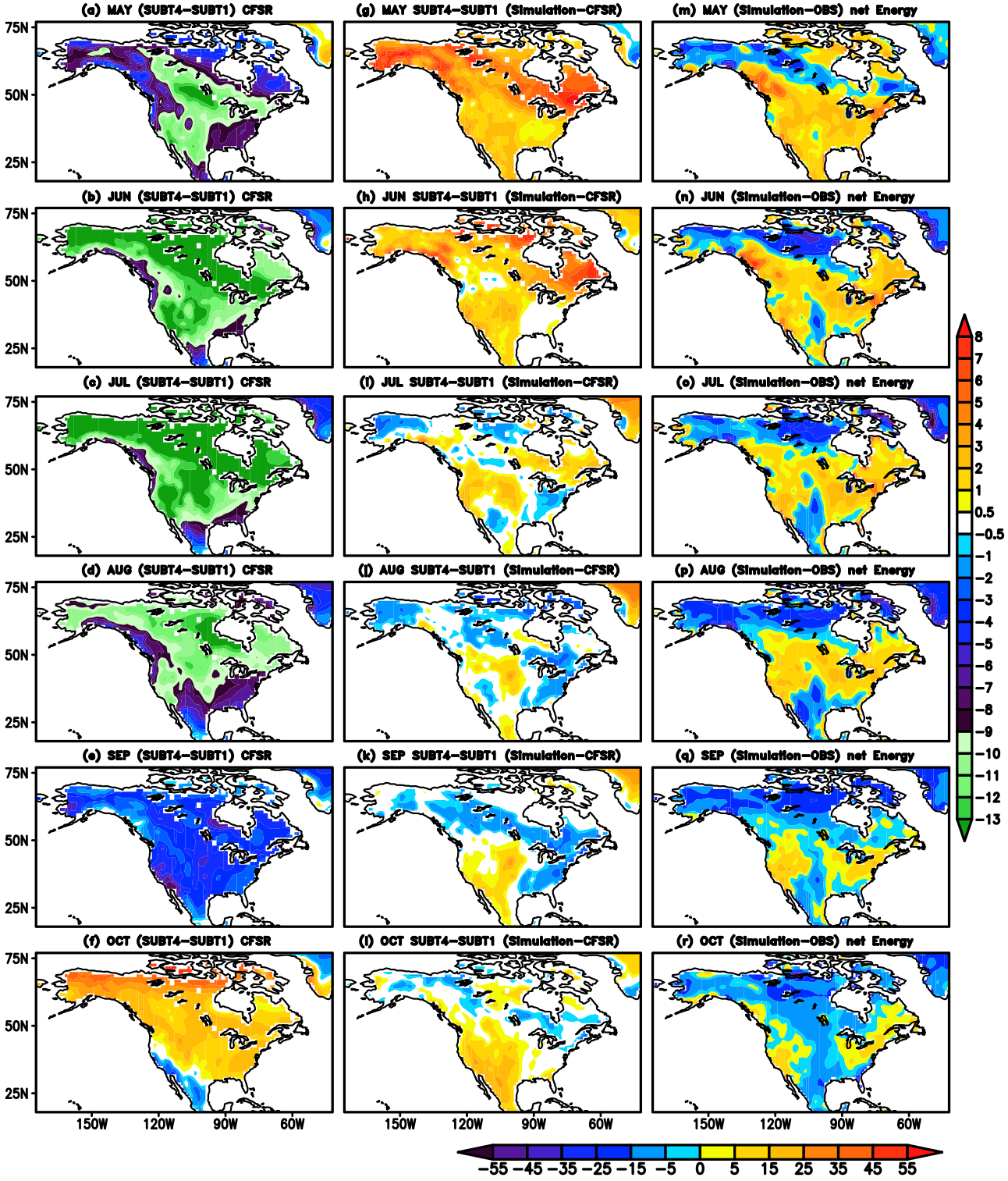

Figure 11. (a–f) Spatial distribution of the climatological difference between SUBT at 100–200 cm and SUBT 0–10 cm in CFSR from May to October over the North America continent. The corresponding model biases are given in Figures 11g–11l. The spatial distributions of monthly net-energy-at-surface climatological biases relative to observation in model simulation during May to October are shown in Figures 11m–11r.

continent. Second, the bias analysis was repeated with monthly means based on the *daily average* of 6-hourly instantaneous values (i.e., 00Z, 06Z, 12Z, and 18Z) in the NCEP CFSv2 FIR and the CFSR (Saha et al., 2010) (Figures S13g–S13l). Our premise is that, if the CFSRR bias with respect to CRU 3.2.1 is similar to that with

respect to CFSR, the CFSv2 FIR bias with respect to CFSR presented in the paper should also be realistic. Given this premise is true, as the third step, we can conduct the bias analysis with monthly means based on the *instantaneous* prognostic fields at 00Z in both the revised version of CFSv2 FIR and the CFSR (Figures S13m–S13r). Our results validated this premise. In fact, we found that the spatial structures of monthly LST bias in the NCEP CFSv2 FIR are similar to those obtained using CRU 3.21 (Figures S13a–S13f) and reanalysis (Figures S13g–S13l). Both feature the cold bias in the eastern part of NA, as well as Alaska and western Canada. To some extent, the spatial structure and magnitude of LST biases at 00Z in both the FIR and reanalysis (Figures S13m–S13r) are similar to those computed based on the daily average of 6-hourly instantaneous values (i.e., 00Z, 06Z, 12Z, and 18Z) and using CRU 3.21, although a mild warm bias appears in the northern latitudes from late spring to early summer.

6. Summary and Discussion

This study investigates the potential impact of deep soil temperature anomalies on the LST during the summer and subsequent seasons over different geographical regions in the NA continent (e.g., the central Great Plains, the NER of NA and the western United States). For this purpose, we have used a 30-year simulation and a set of reforecasts initialized in February and May for period 1979–2008 using a revised version of CFSv2. Our results demonstrate that the model depicts large cold bias at deep soil temperature (100–200 cm) during summer over most of the NA continent. This seasonal bias originates from a remarkably weaker seasonal warming from spring to summer in the model deep soil layer than in observations, although its winter SUBT at 100–200 cm is realistic. The large cold bias in upper soil layer during spring over NER is partly due to an overactive snow-albedo feedback.

Our results demonstrate that the model captures the spatial distribution of reanalysis LST pattern reasonably during spring but depicts large cold bias of 5–9 °C in NER. The simulation also overestimates SCF up to 40% to 70% over NER during spring. Magnitude of SCF bias is larger in simulation in comparison to FIR during March–June. One possible cause for the delayed and slow snow melting in the simulation during March–June over NER in comparison to FIR is discrepancy in location of freezing temperature line between the simulation and the CFSR over the northern AO. During April and May, freezing temperature line in the simulation is still over the northern AO whereas its location is only over land in CFSR and FIR.

Our results demonstrate three distinct evolutions of deep soil temperatures and their influences on the surface temperature in the subregions of the NA continent, the western region, the central Great Plains, and the northeast during summer in the simulation and reforecasts, which are given below:

(i) The model simulation produces excessive snow cover over NER during October to December. The locations of maximum SCF bias shift southeastward during October–December. It may be due to a southward expansion of the frozen ground from September to October in the simulation in comparison to CFSR. As a result, new snow falling on the frozen ground cannot melt and the snow-albedo feedback occurs earlier in the simulation. The model depicts large cold bias at upper soil layer during spring over NER whereas warm bias is found in deep soil layer in simulation. During August–September, the model depicts less cold bias in upper soil layer as it warms up in response to solar heating whereas model deep soil layer has a noticeably smaller seasonal change than the CFSR, resulting in a large cold bias during summer in comparison to the upper one. FIR also depicts large cold bias at deep soil layer in comparison to upper one. As the solar radiation reduces quickly in the early fall, the cold deep soil temperature causes additional cooling in upper soil layer and helps to bring LST to the freezing point early over NER, which allows early snow to accumulate on ground and sets up the stage for a prolonged snow-albedo feedback. As a result, excessive snow cover and cold LST bias persist in this region throughout the winter and spring. Model depicts warm bias in the climatological difference between SUBT at 100–200 cm and SUBT at 0–10 cm over NER in May and June. One of important cause for it is small temperature difference in simulation than that in CFSR because of delay in snow melting. From August to September, the model has negative biases over NER in simulation and reforecasts; it is due to large negative downward temperature gradient in model than in CFSR. The land surface is generally gaining more heat from the atmosphere in simulation than in CFSR over NER during June to August. It may compensate the heat loss from the upper soil layer to the deeper layer.

(ii) During summer, the model simulation depicts cold bias up to 6.0 °C at all the SUBT layers over the central Great Plains during July–September whereas the magnitude of cold bias at all SUBT layers is around

4.0 °C for FIR and 2.5 °C for MIR. The magnitude of cold LST bias is less in comparison to magnitude of the cold SUBT bias in the simulation and reforecasts over the central Great Plains during JAS. Model demonstrates a wet rainfall bias over the central Great Plains in simulation and reforecasts during JAS. Model also depicts large negative bias of SSHF bias and positive bias of SLHF over the central Great Plains during JAS. The latter may also contribute to an excessive summer rainfall during JAS. We may conclude that due to large cold bias from upper soil layer to deep soil layer together over the central Great Plains in simulation and FIR, model may depict large cold bias there.

(iii) The magnitude of LST bias over the western United States is nearly the same in simulation (−2.0 °C), FIR (around −0.4 °C) and MIR (around 1.0 °C) during winter, , and summer, whereas large cold bias is found during summer in SUBT from upper soil layer to deep soil layer in the simulation and reforecasts. A sharp transition in cold bias is also found during spring to summer in SUBT. It is possible that the impact of SUBT on LST over the western USA is negligible in the simulation and reforecasts because oceanic influence is dominant in this region due to stronger upstream marine influence from the Pacific.

The results of this paper provide importance of deep subsurface conditions in the in state-of-the-art coupled general circulation model.

Conflict of Interest

The authors declare that they have no conflict of interest.

Acknowledgments
Funding for this research work was provided by grants from the National Science Foundation (1338427), the National Oceanic and Atmospheric Administration (NA14OAR4310160), and the National Aeronautics and Space Administration (NNX14AM19G). B. Huang is also supported by the NOAA MAPP drought project (NA17OAR4310144). The computations were made on the Extreme Science and Engineering Discovery Environment (XSEDE) high-performance computing platform (Towns et al., 20142014), and the computational resources are gratefully acknowledged. The authors are grateful to two anonymous reviewers for their constructive comments and suggestions, which improved the quality of the manuscript significantly. We would like to share our data to the scientific community that discussed in the manuscript through Zenodo (https://doi.org/10.5281/zenodo.3695951). The CFSR, CERES-EBAF, ERA-Interim, GLDAS-2.0, and ERA40 were respectively obtained from the following sites (https://climatedataguide.ucar.edu/climate-data/climate-forecast-system-reanalysis-cfsr, https://ceres.larc.nasa.gov/products.php?product=EBAF-TOA, https://www.ecmwf.int/en/forecasts/datasets/reanalysis-datasets/era-interim, https://disc.gsfc.nasa.gov/information/news?title=GLDAS%20Version%202.0%20data%20sets%20released%20by%20NASA%20GES%20DISC, https://apps.ecmwf.int/datasets/data/era40-daily/levtype=sfc/).

References

Balmaseda, M., Vidard, A., & Anderson, D. (2008). The ECMWF System 3 ocean analysis system. *Monthly Weather Review*, *136*, 3018–3034.
Balmaseda, M. A., Mogensen, K., & Weaver, A. T. (2013). Evaluation of the ECMWF ocean reanalysis system ORAS4. *Quarterly Journal of the Royal Meteorological Society*, *139*, 1132–1161.
Barnett, T. P., Dumenil, L., Schlese, U., & Roeckner, E. (1988). The effect of Eurasian snow cover on global climate. *Science*, *239*(4839), 504–507. https://doi.org/10.1126/science.239.4839.504
Behringer, D. W. (2005). The Global Ocean Data Assimilation System (GODAS) as NCEP, paper presented at 11th Symposium on Integrated Observing and Assimilation Systems for the Atmosphere, Oceans, and Land Surface, Am. Meteorol. Soc., San Antonio, Tex
Broxton, P. D., Zeng, X., & Dawson, N. (2017). The impact of a low bias in snow water equivalent initialization on CFS seasonal forecasts. *Journal of Climate*, *30*, 8657–8671.
Cohen, J., & Rind, D. (1991). The effect of snow cover on the climate. *Journal of Climate*, *7*, 689–706.
Dee, D. P., Uppala, S. M., Simmons, A. J., Berrisford, P., Poli, P., Kobayashi, S., et al. (2011). The ERA-Interim reanalysis: Configuration and performance of the data assimilation system. *Quarterly Journal of the Royal Meteorological Society*, *137*(656), 553–597. https://doi.org/10.1002/qj.828
Delworth, T. L., & Manabe, S. (1989). The influence of soil wetness on near-surface atmospheric variability. *Journal of Climate*, *2*, 1447–1462.
Dickinson, R. E. (1983). Land surface processes and climate—Surface albedos and energy balance. *Advances in Geophysics*, *25*, 305–353.
Dirmeyer, P. A., & Halder, S. (2017). Application of the land-atmosphere coupling paradigm to the operational Coupled Forecast System (CFSv2). *Journal of Hydrometeorology*, *18*, 85–108. https://doi.org/10.1175/JHM-D-16-0064.1
Douville, H. (2010). Relative contribution of soil moisture and snow mass to seasonal climate predictability: A pilot study. *Climate Dynamics*, *34*, 797–818. https://doi.org/10.1007/s00382-008-0508-1
Dutra, E., Schär, C., Viterbo, P., & Miranda, P. M. A. (2011). Land-atmosphere coupling associated with snow cover. *Geophysical Research Letters*, *38*, L15707. https://doi.org/10.1029/2011GL048435
Ek, M. B., Mitchell, K. E., Lin, Y., Rogers, E., Grunmann, P., Koren, V., et al. (2003). Implementation of Noah land-surface model advances in the NCEP operational mesoscale eta model. *Journal of Geophysical Research*, *108*(D22), 8851. https://doi.org/10.1029/2002JD003296
Fan, X. (2009). Impacts of soil heating condition on precipitation simulations in the weather research and forecasting model. *Monthly Weather Review*, *137*, 2263–2285.
Foster, J., Owe, M., & Rango, A. (1983). Snow cover and temperature relationships in North America and Eurasia. *Journal of Climate and Applied Meteorology*, *22*(460–469), 1983.
Furtado, J. C., Cohen, J. L., Butler, A. H., Riddle, E. E., & Kumar, A. (2015). Eurasian snow cover variability and links to winter climate in the CMIP5 models. *Climate Dynamics*, *45*(9–10), 2591–2605. https://doi.org/10.1007/s00382-015-2494-4
Griffies, S. M., Harrison, M. J., Pacanowski, R. C., & Rosati, A. (2004). Technical guide to MOM4, GFDL Ocean Group Tech. Rep. 5, Geophys. Fluid Dyn. Lab., NOAA, Princeton, N. J. Retrieved from http://www.gfdl.noaa.gov/fms
Guo, Z., Dirmeyer, P. A., Koster, R. D., Sud, Y. C., Bonan, G., Oleson, K. W., et al. (2006). GLACE: The global land–atmosphere coupling experiment. Part II: Analysis. *Journal of Hydrometeorology*, *7*(4), 611–625. https://doi.org/10.1175/JHM511.1
Hahn, D. G., & Shukla, J. (1976). An apparent relationship between Eurasian snow cover and Indian monsoon rainfall. *Journal of the Atmospheric Sciences*, *33*(12), 2461–2462.
Harris, I., Jones, P. D., Osborn, T. J., & Lister, D. H. (2014). Updated high-resolution grids of monthly climatic observations—The CRU TS3.10 dataset. *International Journal of Climatology*, *34*, 623–642. https://doi.org/10.1002/joc.3711
He, Q., Zuo, Z., Zhang, R., & Zhang, R. (2018). Seasonal prediction and predictability of Eurasian spring snow water equivalent in NCEP Climate Forecast System version 2 reforecasts. *Climate Dynamics*, *50*(1–2), 339–348. https://doi.org/10.1007/s00382-017-3611-3
He, Q., Zuo, Z. Y., Zhang, R. H., Yang, S., Wang, W. Q., Zhang, R. N., & Riddle, E. (2016). Prediction skill and predictability of Eurasian snow cover fraction in the NCEP Climate Forecast System version 2 reforecasts. *International Journal of Climatology*, *36*, 4071–4084. https://doi.org/10.1002/joc.4618

Huang, B., Shin, C. S., Shukla, J., Marx, L., Balmaseda, M., Halder, S., et al. (2017). Reforecasting the ENSO events in the past fifty-seven years (1958–2014). *Journal of Climate*, *30*(19), 7669–7693. https://doi.org/10.1175/JCLI-D-16-0642.1

Huang, B., Zhu, J., Marx, L., Wu, X., Kumar, A., Hu, Z. Z., et al. (2015). Climate drift of AMOC, North Atlantic salinity and Arctic sea ice in CFSv2 decadal predictions. *Climate Dynamics*, *44*, 559–583. https://doi.org/10.1007/s00382-014-2395-y

Kim, Y., & Wang, G. (2007). Impact of initial soil moisture anomalies on subsequent precipitation over North America in the coupled land–atmosphere model CAM3-CLM3. *Journal of Hydrometeorology*, *8*, 513–533.

Koster, R. D., Dirmeyer, P. A., Guo, Z., Bonan, G., Chan, E., Cox, P., et al., & GLACE Team (2004). Regions of strong coupling between soil moisture and precipitation. *Science*, *305*(5687), 1138–1140. https://doi.org/10.1126/science.1100217

Koster, R. D., Mahanama, S. P. P., Yamada, T. J., Balsamo, G., Berg, A. A., Boisserie, M., et al. (2010). The contribution of land surface initialization to subseasonal forecast skill: first results from multi-model experiment. *Geophysical Research Letters*, *37*, L02402. https://doi.org/10.1029/2009GL041677

Koster, R. D., Mahanama, S. P. P., Yamada, T. J., Balsamo, G., Berg, A. A., Boisserie, M., et al. (2011). The second phase of the global land–atmosphere coupling experiment: Soil moisture contributions to subseasonal forecast skill. *Journal of Hydrometeorology*, *12*(5), 805–822. https://doi.org/10.1175/2011JHM1365.1

Koster, R. D., & Suarez, M. J. (2003). Impact of land surface initialization on seasonal precipitation and temperature prediction. *Journal of Hydrometeorology*, *4*, 408–423.

Mahanama, S. P. P., Koster, R. D., Reichle, R. H., & Suarez, M. J. (2008). Impact of subsurface temperature variability on surface air temperature variability: An AGCM study. *Journal of Hydrometeorology*, *9*(4), 804–815. https://doi.org/10.1175/2008JHM949.1

Peng, P., Barnston, A. G., & Kumar, A. (2012). A comparison of skill between two versions of the NCEP Climate Forecast System (CFS) and CPC's operational short-lead seasonal outlooks. *Weather and Forecasting*, *28*, 445–462.

Rodell, M., Houser, P. R., Jambor, U., Gottschalck, J., Mitchell, K., Meng, C.-J., et al. (2004). The global land data assimilation system. *Bulletin of the American Meteorological Society*, *85*(3), 381–394.

Roesch, A. (2006). Evaluation of surface albedo and snow cover in AR4 coupled climate models. *Journal of Geophysical Research*, *111*, D15111. https://doi.org/10.1029/2005JD006473

Roundy, J. K., Ferguson, C. R., & Wood, E. (2014). Impact of land-atmospheric coupling in CFSv2 on drought prediction. *Climate Dynamics*, *43*, 421–434.

Saha, S., Moorthi, S., Pan, H. L., Wu, X., Wang, J., Nadiga, S., et al. (2010). The NCEP climate forecast system reanalysis. *Bulletin of the American Meteorological Society*, *91*(8), 1015–1058. https://doi.org/10.1175/2010BAMS3001.1

Saha, S., Moorthi, S., Wu, X., Wang, J., Nadiga, S., Patrick, T., et al. (2014). The NCEP Climate Forecast System version 2. *Journal of Climate*, *27*, 2185–2208.

Santanello, J. A. Jr., Dirmeyer, P. A., Ferguson, C. R., Findell, K. L., Tawfik, A. B., Berg, A., et al. (2018). Land–atmosphere interactions: The LoCo perspective. *Bulletin of the American Meteorological Society*, *99*(6), 1253–1272. https://doi.org/10.1175/BAMS-D-17-0001.1

Seneviratne, S. I., Corti, T., Davin, E. L., Hirschi, M., Jaeger, E. B., Lehner, I., et al. (2010). Investigating soil moisture–climate interactions in a changing climate: A review. *Earth Science Reviews*, *99*(3-4), 125–161. https://doi.org/10.1016/j.earscirev.2010.02.004

Seneviratne, S. I., Luthi, D., Litschi, M., & Schär, C. (2006). Land atmosphere coupling and climate change in Europe. *Nature*, *443*(7108), 205–209. https://doi.org/10.1038/nature05095

Shukla, J., & Mintz, Y. (1982). Influence of land-surface evapotranspiration on the earth's climate. *Science*, *215*(4539), 1498–1501. https://doi.org/10.1126/science.215.4539.1498

Shukla, R. P., & Huang, B. (2015). Mean state and interannual variability of the Indian summer monsoon simulation by NCEP CFSv2. *Climate Dynamics*, *46*(11-12), 3845–3864. https://doi.org/10.1007/s00382-015-2808-6

Shukla, R. P., Huang, B., Dirmeyer, P. A., & Kinter, J. L. (2019). The influence of summer deep soil temperature on early winter snow conditions in Eurasia in the NCEP CFSv2 Simulation. *Journal of Geophysical Research: Atmospheres*, *124*, 9062–9077. https://doi.org/10.1029/2019JD030279

Shukla, R. P., Huang, B., Dirmeyer, P. A., Kinter, J. L., Shin, C.-S., & Marx, L. (2019). Climatological influence of Eurasian winter surface condition on the Asian and Indo-Pacific summer circulation in the CFSv2 seasonal reforecasts. *International Journal of Climatology*, *39*(8), 3431–3453. https://doi.org/10.1002/joc.6029

Shukla, R. P., Huang, B., Marx, L., Kinter, J. L., & Shin, C.-S. (2017). Predictability and prediction of Indian summer monsoon by CFSv2: Implication of the initial shock effect. *Climate Dynamics*, *50*(1-2), 159–178. https://doi.org/10.1007/s00382-017-3594-0

Towns, J., Cockerill, T., Dahan, M., Foster, I., Gaither, K., Grimshaw, A., et al. (2014). XSEDE: Accelerating scientific discovery. *Computing in Science & Engineering*, *16*(5), 62–74. https://doi.org/10.1109/MCSE.2014.80

van den Hurk, B. J. J. M., Best, M., Dirmeyer, P., Pitman, A., Polcher, J., & Santanello, J. Jr. (2011). Acceleration of land surface model development over a decade of GLASS. *Bulletin of the American Meteorological Society*, *92*, 1593–1600. https://doi.org/10.1175/BAMS-D-11-00007.1

van den Hurk, B., Doblas-Reyes, F., Balsamo, G. Koster R. D., Seneviratne S. I., & Camargo H. Jr. (2012). Soil moisture effects on seasonal temperature and precipitation forecast scores in Europe. *Climate Dynamics 38*, 349–362. https://doi.org/10.1007/s00382-010-0956-2

Wielicki, B. A., Barkstrom, B. R., Harrison, E. F., Lee, R. B. III, Louis Smith, G., & Cooper, J. E. (1996). Clouds and the Earth's Radiant Energy System (CERES): An earth observing system experiment. *Bulletin of the American Meteorological Society*, *77*(5), 853–868. https://doi.org/10.1175/1520-0477(1996)077<0853:CATERE>2.0.CO;2

Winton, M. (2000). A reformulated three-layer sea ice model. *Journal of Atmospheric and Oceanic Technology*, *17*, 525–531. https://doi.org/10.1175/1520-0426(2000)017<0525:ARTLSI>2.0.CO;2

Wu, L. Y., & Zhang, J. Y. (2014). Strong subsurface soil temperature feedbacks on summer climate variability over the arid/semi-arid regions of East Asia. *Atmospheric Science Letters*, *15*(4), 307–313.

Xue, Y., Diallo, I., Li, W., David Neelin, J., Chu, P. C., Vasic, R., et al. (2018). Spring land surface and subsurface temperature anomalies and subsequent downstream late spring-summer droughts/floods in North America and East Asia. *Journal of Geophysical Research: Atmospheres*, *123*, 5001–5019. https://doi.org/10.1029/2017JD028246

Xue, Y., Oaida, C. M., Diallo, I., Neelin, J. D., Li, S., de Sales, F., et al. (2016). Spring land temperature anomalies in northwestern US and the summer drought over Southern Plains and adjacent areas. *Environmental Research Letters*, *11*(4), 044018. https://doi.org/10.1088/1748-9326/11/4/044018

Xue, Y., Vasic, R., Janjic, Z., Liu, Y. M., & Chu, P. C. (2012). The impact of spring subsurface soil temperature anomaly in the western U.S. on North American summer precipitation—A case study using regional climate model downscaling. *Journal of Geophysical Research*, *117*, D11103. https://doi.org/10.1029/2012JD017692

Yasunari, T., Kitoh, A., & Tokioka, T. (1991). Local and remote responses to excessive snow mass over Eurasia appearing in the northern spring and summer climate—A study with the MRI GCM. *Journal of the Meteorological Society of Japan*, *69*, 473–487.